Garcia-Mulero, A.; Rendón-Patiño, A.; Asiri, AM.; Primo Arnau, AM.; García Gómez, H. (2021). Band Engineering of Semiconducting Microporous Graphitic Carbons by Phosphorous Doping: Enhancing of Photocatalytic Overall Water Splitting. ACS Applied Materials & Interfaces. 13(41):48753-48763. https://doi.org/10.1021/acsami.1c14357

Band engineering of semiconducting microporous graphitic carbons by phosphorous doping: enhancing of photocatalytic overall water splitting

Ana García-Mulero[a], Alejandra Rendón-Patiño[a], Abdullah M. Asiri[b], Ana Primo[a*] and Hermenegildo Garcia[a*]

[a]Instituto de Tecnología Química, Consejo Superior de Investigaciones Científicas-Universitat Politecnica de Valencia, Universitat Politécnica de Valencia, Av. De los Naranjos s/n, 46022 Valencia, Spain.

[b]Center of Excellence for Advanced Materials, King Abdulaziz University, Jeddah, Saudi Arabia

Abstract

Carbon-based solar photocatalysts for overall water splitting could provide H_2 as energy vector in a clean and sustainable way. Band engineering to align energy levels can be achieved, among other ways, by doping. Herein, it is shown that phosphorous doping of microporous graphitic carbons derived from pyrolysis of α–, β– and γ-cyclodextrin increases the valence band edge energy of the material, and the energy value of the conduction band decreases with the P content. In this way, P doping increases the activity of these metal-free materials in the photocatalytic overall water splitting under simulated sunlight and visible light illumination. The optimal material reaches, under simulated one sun irradiation in 4 h, a H_2 production in the absence of metals of 2.5 mmol $H_2 \times g_{catalyst}^{-1}$ in the presence of methanol and 225 μmol $H_2 \times g_{catalyst}^{-1}$ from H_2O in the absence of any sacrificial electron donor.

Introduction

Implementation of the hydrogen technology requires of efficient ways to generate this energy vector from water using renewable energy.[1, 2] Photocatalytic overall water splitting using sunlight could be a viable strategy to achieve this goal, provided that affordable, efficient and durable photocatalysts are developed.[3] Since the seminal study of Fujishima and Honda showing the photoelectrocatalytic activity of TiO_2 under UV light illumination,[4] much research has been focused on the study of the photocatalytic activity of inorganic semiconductors for overall water splitting.[5] However, recent updates of critical raw materials include titanium and strontium as elements with limited resources in comparison with their growing demand.[6] Thus, it seems reasonable to move towards sustainable and renewable photocatalysts.

Besides inorganic semiconductors, it has been found that carbon nitrides can act as metal-free photocatalysts for the generation of hydrogen with different efficiencies depending on the preparation procedure, the crystallinity of the resulting sample and the presence of defects, among other parameters.[7, 8] In this context, the wide availability of defective graphenes and their heterojunctions combined with their semiconducting properties have open the door for the use also of this type of 2D nanomaterials as metal-free photocatalysts.[9, 10] Besides sustainability and abundance, an additional advantage of carbon-based photocatalysts is their easy structural modification and doping. Both factors can alter band alignment and may result in an enhancement of their photocatalytic activity.[11]

Following the lead of graphene oxide that is a wide bandgap metal-free semiconductor with response exclusively in the UV region,[12] it was found that doping with heteroatoms on defective graphenes introduces photocatalytic activity upon solar and visible light irradiation.[13] The photocatalytic activity of these defective doped graphenes increases also upon deposition of metal nanoparticles as co-catalysts.[14]

In this context, we have recently reported the preparation of a novel type of structured microporous graphitic carbon [mp-C, mp- meaning microporous, C corresponding to graphitic carbon] with semiconducting properties by pyrolysis of cyclodextrins.[15] The special molecular geometry of cyclodextrins having a truncated conical structure with a hollowed interior determines their self-assembly, probably in the melt state above 300 ^{o}C, during the thermal treatment leading to graphitization. The resulting graphitic carbon is constituted by nanoparticles about 20-30 nm diameter having channels with a strictly regular microporosity. The micropore dimension is a function of the number of glucopyranosyl units of the cyclodextrin precursor.[16] The resulting mp-C materials may have a carbon percentage over 95 %, with a low residual O content, much lower than those achieved in the pyrolysis of linear oligo- and polysaccharides resulting in 2D sheets that is typically about 15 %.[16] it was demonstrated that microporosity and pore size play a key role in the activation of O_2 and other small molecules such as H_2O compared to analogous flat 2D graphene sheets.

Considering that for photocatalytic applications band alignment is of paramount importance and that heteroatom doping is a general strategy to tune the position of the frontier bands,[17] it is of interest to determine what is the influence of doping on the

photocatalytic activity of these microporous, structured graphitic mp-C materials for H_2 generation from H_2O.

Following the lead of defective graphenes as photocatalysts in which phosphorous is a suitable dopant element to increase the photocatalytic activity of 2D layered graphene nanomaterials,[18] herein, it will be reported that P-doping influences the band alignment of microporous graphitic C [mp-(P)C]. Under optimal conditions the mp-(P)C exhibits much enhanced photocatalytic activity for overall water splitting under simulated sunlight illumination as compared to the parent mp-C material, reaching values that are among the highest ever reported for a C-based photocatalyst in the absence of any metal for overall water splitting. As for the parent mp-C materials,[15] an influence of the pore size on the photocatalytic activity has been observed for mp-(P)C, the most active material being the one with the smallest pore diameter.

Results and discussion

Materials preparation and characterization.

As a source of phosphorous for the doping, two different P-containing compounds, either phosphoric or phytic acid, were used. Phosphoric acid forms esters with saccharide hydroxyl groups and has been reported to dope defective graphene with P,[18] and phytic acid forms a defective P-doped graphitic carbon.[10] These chemicals were physically mixed with the corresponding α–, β– or γ–cyclodextrin, before submitting the mixture to pyrolysis

in a horizontal tubular, electrical furnace under Ar atmosphere at 900 ºC. Chemical analysis of the resulting mp-C materials confirmed the presence of P element. The P percentage depends on the weight of P precursor compound mixed with cyclodextrin. Table 1 summarizes the composition of some of the (P)C samples prepared in the present study.

Table 1. Composition of microporous graphitic carbon obtained by pyrolysis of α-, β-, and γ- cyclodextrins with different amounts of the phosphorous source.[a]

Sample	% C	% P	Surface area[c] ($m^2 x\ g^{-1}$)	Band gap (eV)
C_α	95.44	0	727.5	3.30
(P)C_α-1	79.85	0.14	-	4.50
(P)C_α-2	71.77	2.40	1927.6	3.16
(P)C_α-3	55.17	2.40	-	3.07
(P)C_α-4[b]	75.05	1.56	1572.7	3.24
(P)C_β–2	73.95	1.37	1149.7	3.28
(P)C_γ–2	77.38	3.25	1619.4	3.01

[a] C percentage was obtained by combustion elemental analysis and P amount by XPS and ICP-OES. Oxygen percentage is assumed as the residual to 100 %. [b] Phytic acid as P precursor in this sample, while phosphoric acid was the precursor of the other samples. [c] Measured from CO_2 adsorption.

A remarkable influence of the use of phosphoric acid as source of P atoms in doping is the remarkable increase in the specific surface area of the resulting (P)C materials, much more than the double of that of the parent C_α and closer to the theoretical value for single layer graphene (Table 1 and Fig. S.1). A clear effect of the presence of P as dopant element can be observed in the thermogravimetric profiles of mp-(P)C samples (Figs. S2-S5). Upon

heating under air, the sample weight increases up to temperatures of 550 ^{o}C, a fact that can be attributed to the incorporation of oxygen to the samples due to the oxidation of P atoms. After that the sample experiences a weight loss corresponding to the combustion of the C matrix finishing at 700 ^{o}C. This decomposition temperature is much higher than that of undoped mp-C that occurs at about 500 ^{o}C.[16]

The graphitic nature of the mp-(P)C materials was assessed by Raman spectroscopy. These Raman spectra show the presence of the characteristic G and D bands of defective graphite at 1590 and 1350 cm^{-1}, respectively, accompanied by a less-intense, very broad absorption band from 3250 to 2500 cm^{-1}, due to overtone and combination vibrations.[19] The relative intensity of the G vs. the D band was about 1.15-1.25 that is in the expected range for graphitic carbons derived from carbohydrate pyrolysis.[20] Fig. S.6 in supporting information shows the Raman spectra recorded for the samples under study.

The graphitic nature of the mp-(P)G samples and their microporosity was clearly observed by TEM images. Fig. 1 shows selected images of mp-(P)C$_{\alpha}$ and mp-(P)C$_{\beta}$ to illustrate the structure of the samples that was similar for all mp-(P)C samples regardless the P content or the cyclodextrin precursor. As previously reported for the case of mp-C, the mp-(P)C samples are constituted by microporous carbon nanoparticles of dimensions about 20-30 nm. These images show the presence of regular, microporous parallel channels in the particles. From the periodic variation of the contrast between the walls and the pores, the diameters of the channels can be measured. It was determined that for (P)C$_{\alpha}$-2 derived from α-cyclodextrin the pore diameter was 0.66 nm, while the pore dimensions of (P)C$_{\beta}$–2 and (P)C$_{\gamma}$–2 using β- and γ-cyclodextrin as precursors were 0.97 and 1.32 nm, respectively.

Thus, the pore dimensions of the cyclodextrin precursor and their different size (5.7, 7.8 and 9.5 Å for α, β and γ, respectively) is reflected also on the pore dimensions of the resulting mp-(P)C material. Importantly, the presence of independent particles attributable to phosphoric or phytic acids could not be detected on the samples by TEM. Of note is that mp(P)C form persistent dispersions in water with mononodal particle size distribution as determined by dynamic laser scattering and average diameter larger (about 100 nm, Fig. S.7) than that measured by TEM. At neutral pH values, the surface has abundant negative charge density probably due to the presence of carboxylate or phosphate groups with a zeta potential above -45 mV, in agreement with the dispersion stability.

mp-(P)C samples exhibit characteristic XRD patterns with broad peaks at 24 (002) and 42 º (101) corresponding to the poorly crystalline graphitic carbons, but in which the presence of other sharper peaks at smaller angles below 15 º can also be recorded. As an example Fig. 1 also shows the XRD patterns for (P)C_{α}-2 and (P)C_{β}-2. The presence of these short angle diffraction peaks have been attributed to the narrow pore size of the microporous channels derived from cyclodextrin fusion as shown in the TEM images.

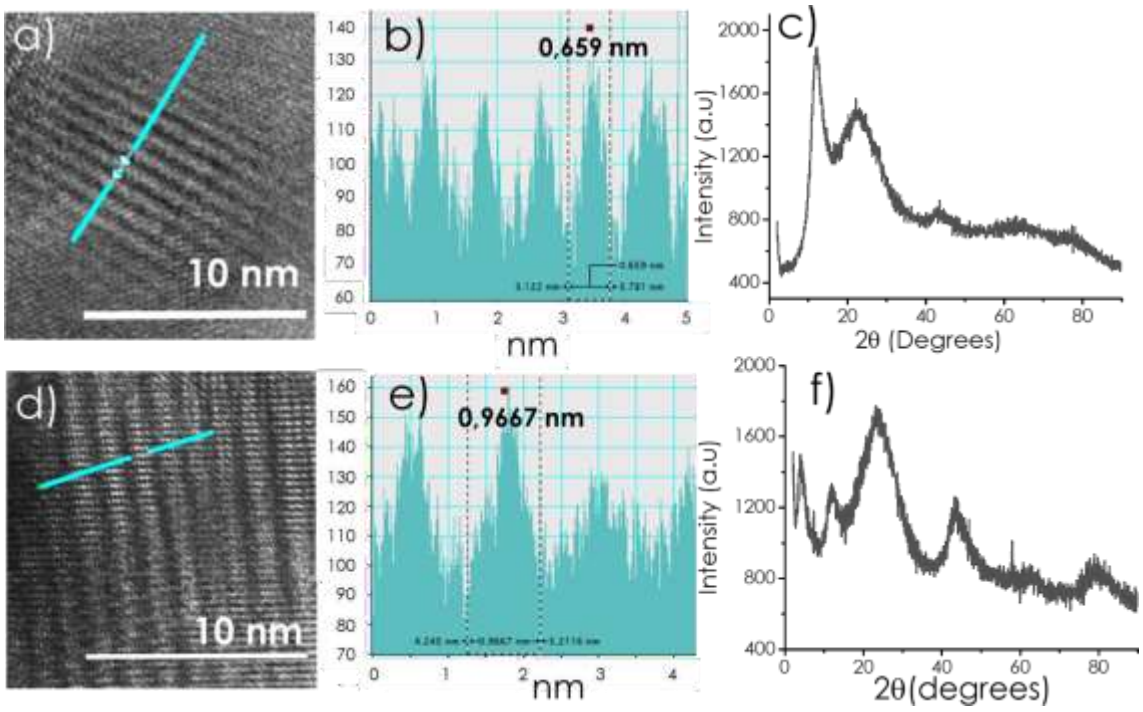

Fig. 1. TEM images of a, b, c) (P)C_α-2 and d, e, f) (P)C_β–2. Panels b and e show the periodic contrast across the blue line of the TEM images in a and d. From these measurements a pore dimension of 0.66 and 0.97 nm was estimated for (P)C_α-2 and (P)C_β-2, respectively. c) and f) XRD patterns of PC_α-2 and PC_β-2 samples.

Solid-state ^{31}P NMR spectra of the mp-(P)C samples show the presence of a sharp peak at about 0 ppm, accompanied by a broader less intense peak at about 35 ppm. Illustrative examples are presented in Fig. 2. These chemical shifts agree well with the values of triphenylphosphine (7.3 ppm) and triphenylphosphine oxide (29.4 ppm) and would indicate the presence of two major types of P atoms on mp-(P)C materials. Accordingly, one of them would correspond to graphitic P and the other to the P oxide, resulting from the complete or incomplete reduction of phosphate groups, respectively. The occurrence of

chemical reduction under pyrolysis conditions is a well-known fact and results, for instance, in the formation of metal nanoparticles from their corresponding metal salts.[21, 22]

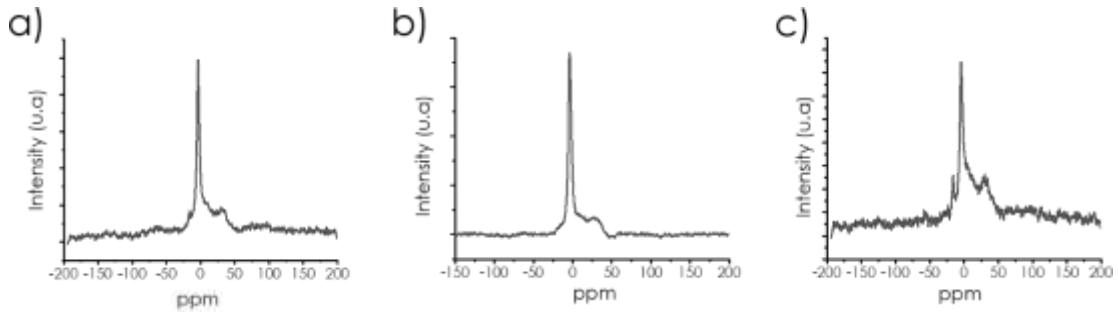

Fig. 2. Solid-state MAS ^{31}P NMR spectra of (P)C$_\alpha$-2 (a), (P)C$_\beta$–2 (b), and (P)C$_\gamma$–2 (c) showing a main type of graphitic P (CCCP) at about 0 ppm, accompanied by some residual (CCC)P=O component appearing at about 35 ppm.

Figs. 3 and S8 show the experimental high-resolution XPS C1s and P2p peaks recorded for the mp-(P)C samples as well as the best deconvolution to individual components. As it can be seen in these spectra, C1s has three components at 283.6, 284.5 and 288.0 eV attributable to the C atoms bonded to P, graphitic C and C atoms bonded to O. Note that the first two components were the prevalent ones, indicating the occurrence of P doping. In the XPS P2p peak, the experimental peaks fit well with two components corresponding to graphenic P and P atoms bonded to one O and three C atoms appearing at binding energies of 131.5 and 132.8 eV, respectively.

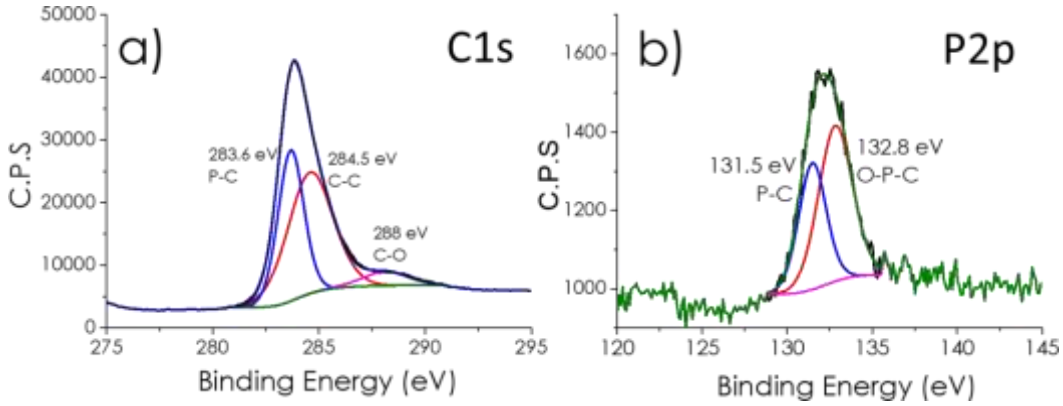

Fig. 3. High-resolution XPS C1s and P2p peaks and their best fit to individual components (as indicated in the spectra) obtained for sample (P)Cα-2.

Optical bandgap of the resulting mp-(P)C samples were estimated from the Tauc plots of the diffuse reflectance UV-Vis absorption spectra (Fig. S.9). Bandgap energy values were determined by extrapolation of the linear part of these spectra and were in the range from 3.01 to 4.50 eV. The bandgap energy values for the samples under study are collected in Table 1. The energy of the valence band edges was determined by XPS by measuring the minimum energy to detect electrons, correcting the value according to the work function of the instrument (see Fig. S9 and supporting information for details). Fig. 4 illustrates the valence and conduction band energy of (P)C$_\alpha$ series compared to that of the undoped mp-C$_\alpha$ sample. Interestingly, P doping increases the valence band energy values, probably reflecting the contribution of lone electron pairs of P atoms to this state increasing their energy. The reduction potential of the conduction band is also increased by P doping, but it decreases along the P content becoming similar to that of undoped mp-C.

Overall Figure 4 shows the validity of the concept of the present research to tune the frontier orbitals of a semiconducting carbon material by P doping. Although all the materials have conduction and valence band potentials adequate for overall water splitting at neutral pH (as it is experimentally observed), (P)C$_\alpha$-2 is the one that has better alignment with overall water splitting. This is because (P)Cα-2 has the narrower band gap, while the frontier band energy values are well aligned with those of HER and OER at neutral pH plus a kinetic overpotential estimated in a minimum of -/+ 0.3 V. In contrast, further doping as in (P)C$_\alpha$-3 decreases the reduction potential of the conduction band electrons, positioning it at the lowest value.

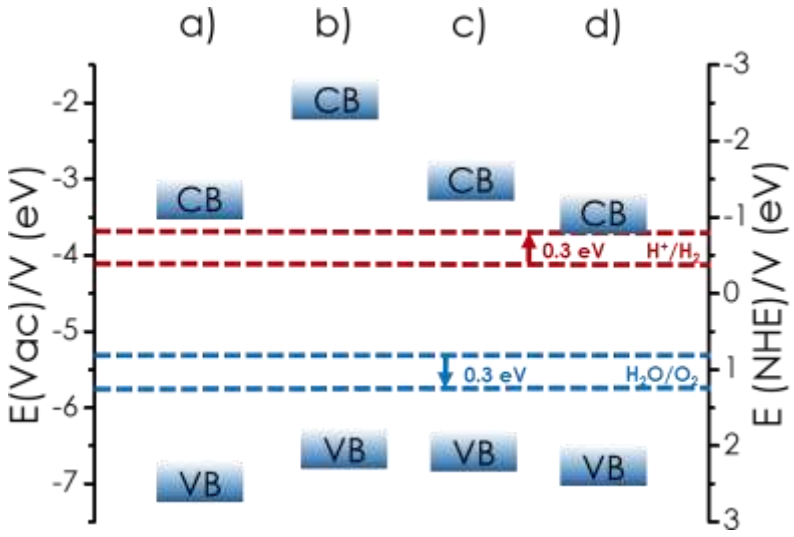

Fig. 4. Valence and conduction band energy values for a) C$_\alpha$, b) (P)C$_\alpha$-1, c) (P)C$_\alpha$-2 and d) (P)C$_\alpha$-3 in comparison with the thermodynamic values of the HER and OER potentials at neutral pH and the HER and OER with increased over potentials.

Photocatalytic hydrogen evolution activity.

Photocatalytic experiments were carried out with solid photocatalysts in suspension under magnetic stirring in a sealed quartz photoreactor under simulated sunlight irradiation at about one Sun power. Preliminary controls in the dark allowed detecting some minor H_2 evolution. This negligible H_2 evolution can be attributed to the presence of some residual elemental P undergoing spontaneous oxidation by H_2O and releasing H_2 in the process. Elemental P would be produced during the pyrolysis as consequence of the previously-commented reducing conditions of the thermal treatment in which evolution of CO_2, CO and H_2O gases takes place. The term carbochemical reduction has been coined to indicate that metal salts, such as Ni^{2+} or Cu^{2+}, become reduced to the metallic elements in the pyrolysis.[21, 22] It is proposed that similar chemical reduction of phosphate groups should occur, forming a minor amount of elemental P, concomitantly with the P doping of the nascent mp-(P)C. The amount of elemental P on mp-(P)C has to be, however, necessarily small since elemental P sublimes at the high temperatures of the pyrolysis under a continuous Ar flow. Not surprisingly, the dark H_2 production lower than 0.05 $mmol \times g_{catalyst}^{-1}$ was minor compared to the H_2 evolved upon irradiation as presented in Fig. 5.

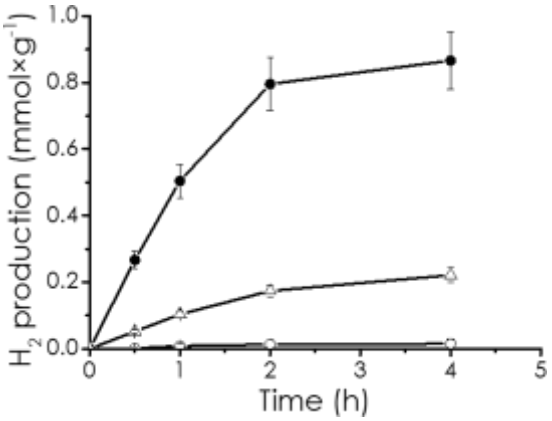

Fig. 5. Temporal H_2 evolution profiles for (P)C$_\alpha$-2 (○ in the dark, ● under irradiation) and mp-C$_\alpha$ (△). Reaction conditions: 4:1 H_2O (MilliQ quality)-methanol suspension in a reactor of 51 mL, irradiation using 300 W Xe lamp with AM 1.5 filter at room temperature. The error bars have been estimated from independent experiments.

The initial photocatalytic experiments were aimed at determining the optimal weight percentage of mp-(P)C$_\alpha$ for the maximum hydrogen evolution in a 4:1 H_2O-methanol suspension. Under the present irradiation conditions, no linear relationship between H_2 evolution and photocatalyst mass is observed. Fig. 6 presents the time-conversion plots for the various photocatalyst concentrations studied in the range from 0.1 to 2.0 mg catalyst$\times$mL^{-1}. The maximum H_2 evolution was measured for 0.5 mg catalyst$\times$mL^{-1} of solution that reached 14 μmol H_2 in 24 h, corresponding to 1.4 mmol $H_2 \times g_{catalyst}^{-1}$. Higher or lower amounts of (P)C$_\alpha$ giving lower H_2 production. The existence of an optimal material amount to achieve the optimal response has been commonly observed in photocatalysis and has been interpreted as derived from the combination of two opposite effects. On one

hand, an increase of photocatalyst amount is positive due to an increase of light harvesting and the higher number of electrons and holes that are generated. On the other hand, high photocatalyst concentrations decrease light penetration in the suspension and this lack of transparency leads to an inefficient irradiation of the whole suspension. It is worth commenting that if the H_2 production is divided by the photocatalyst mass, rather than the absolute evolved H_2 mols, then, the most efficient concentration was 0.1 $mg \times mL^{-1}$, resulting in a H_2 production over 3.2 mmol $H_2 \times g_{catalyst}^{-1}$ in 24 h. This H_2 production value is remarkable and compares favorably with similar values reported in the literature.[23-26] However, as mentioned earlier, the response of the photocatalytic H_2 evolution with the mass is not linear in the range under consideration. Therefore, it is worth noting that an increase of the mass by a factor of ten is not accompanied by an increase by the same factor in the H_2 production (see Fig. 6). Thus, a concentration of 0.5 $mg \times mL^{-1}$ that produces the highest absolute evolved H_2 mols was selected in subsequent studies.

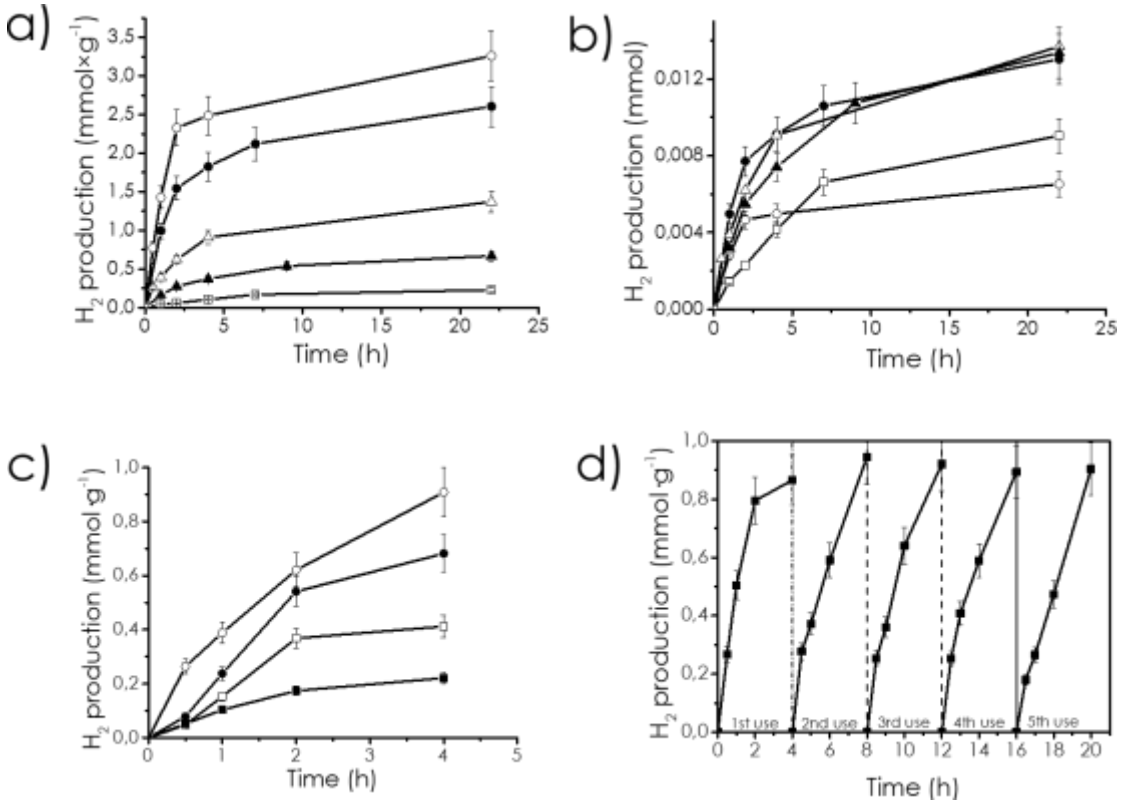

Fig. 6. Temporal profiles of hydrogen evolution plotted as a) mmol of H_2 per g or b) the absolute evolved H_2 mmols using different photocatalyst concentration of (P)C$_\alpha$-2: ○) 0.1 mg×mL^{-1}, ●) 0.25 mg×mL^{-1}, △) 0.5 mg×mL^{-1}, ▲) 1 mg×mL^{-1}, □) 2 mg×mL^{-1} ; c) H_2 evolution using mp-(P)C resulting from different cyclodextrin precursors at a concentration of 0.5 mg×mL^{-1}: ○) (P)C$_\alpha$-2, ●) (P)C$_\beta$-2, □) (P)C$_\gamma$-2, ■) mp-C$_\alpha$, and d) reuses of (P)C$_\alpha$-2. Reaction conditions: 4:1 H_2O (MilliQ quality)-methanol suspension in a reactor of 51 mL, irradiation using 300 W Xe lamp with AM 1.5 filter at room temperature. The error bars have been estimated from independent experiments.

The positive influence of P doping on the photocatalytic activity of mp-C_α was assessed in the presence of sacrificial agent by comparing under identical conditions the performance of mp-C_α prepared following identical preparation procedure as that of mp-(P)C_α, but in the absence of a source of P. The results presented in Fig. 5 show that the H_2 evolution increases by a factor of five for mp-(P)C_α as compared to mp-C_α, thus providing an additional example of doping as a general strategy to increase the photocatalytic activity in graphitic materials. This higher photocatalytic activity derives from the narrower band gap of (P)C_α-2 allowing more efficient light harvesting and the appropriate band alignment.

The influence of the pore size of mp-(P)C on the photocatalytic activity was studied by comparing the performance of a series of mp-(P)C samples derived from α–, β– and γ-cyclodextrins at the similar P doping level. It was observed that the relative photocatalytic activity follows the order mp-(P)C_α > mp-(P)C_β > mp-(P)C_γ. This is in line with the previous observation of the positive influence of small pore size on the (photo)catalytic activity.[15 16] This relative photocatalytic activity order was also measured at various P contents, showing the positive influence of H_2O confinement and small pore size on the photocatalytic reaction.

Regarding the influence of P doping for (P)C_β and (P)$C\gamma$, their photoresponse increases with P loading in the range under study. This trend is similar to that observed for (P)C_α, although the relative influence of P doping was less important as the pore size increases. Fig S.11 in Supporting information provides the temporal profiles for the series of mp-(P)C at different P contents.

Stability of the photocatalytic activity of mp-(P)Cα under irradiation conditions in the presence of methanol as sacrificial electron donor was assessed by performing a series of consecutive runs using the same sample, monitoring the temporal H_2 evolution in each reaction. After each reaction, the solid photocatalyst was recovered from the suspension by centrifugation and washed exhaustively with water to remove remaining methanol and possible by-products. The results are presented in Fig. 6. As it can be seen there, no changes in the initial reaction rate or H_2 production at 4 h irradiation time were monitored in five consecutive reuses, proving stability of the photocatalytic activity.

According to solid-state ^{31}P-NMR and XP spectroscopy, dopant P atoms can be present in two major coordination modes. The distribution of P atoms in the two families depends, among other possible parameters, on the compound used as source of P. A comparison of the photocatalytic activity for H_2 evolution in the presence of methanol as sacrificial electron donor indicates that, at similar P doping level, the mp-(P)Cα material obtained from phosphoric acid was more efficient that the analogous sample prepared from phytic acid (Fig. S.12 in Supporting information). Thus, subsequent measurements were performed using phosphoric acid as source of P. This influence of the P precursor can be attributable to the various percentages of P distribution on difference in the specific surface area (see Table 1).

Photoresponse of mp-(P)Cα as a function of the wavelength range was studied using methanol as sacrificial electron donor. Photocatalytic H_2 generation under irradiation of the full output of a Xe lamp was compared with that of a solar simulator and visible light. The temporal evolution of the full Xe lamp output and simulated solar light was similar after

correction for the higher power intensity of the Xe lamp. Comparison of the photocatalytic hydrogen evolution in the presence of methanol as sacrificial electron donor for mp-(P)C_α upon simulated solar light or under visible light (λ>420 nm) irradiation indicates that although mp-(P)C_α has visible light photoresponse, about half of its photocatalytic activity derives from the UV region of the solar spectrum. This behavior is not uncommon and has been previously observed in other carbonaceous materials that exhibit higher activity for UV photons compared to the less energetic visible radiation due to their bandgap value about 3 eV. Fig S.13 in supporting information presents the temporal profile of H_2 evolution for simulated sunlight and UV-filtered radiation.

Photocatalytic overall H_2O splitting.

Photocatalytic O_2 evolution is thermodynamically and kinetically more demanding than H_2 generation. Therefore, it was of interest to determine what is specifically the influence of P-doping on this semireaction. To facilitate the process, the photocatalytic activity for O_2 evolution of mp-(P)C_α was initially tested in the presence of Ce^{IV} as sacrificial electron acceptor, whereby a continuous O_2 production along the irradiation time was measured. Fig. 7 shows the temporal O_2 evolution in the presence of mp-(P)C as photocatalyst. These measurements experimentally show that the valence band holes in mp-(P)C_α have enough potential to promote H_2O oxidation.

Accordingly, mp-(P)C_α was tested as photocatalyst for overall H_2O splitting under simulated sunlight irradiation in the absence of sacrificial agents. Although a certain delay in the observation of O_2 respect to H_2 was observed at short irradiation times, the temporal

profiles of H_2 and O_2 shown also in Fig. 7 indicate that both gases evolve from pure water under continuous irradiation reaching a final productivity at 20 h of 300 μmol $H_2 \times g_{catalyst}^{-1}$. This productivity in overall water splitting is remarkable considering the absence of any metal acting as co-catalyst favoring charge separation and gas evolution and is much higher than that observed for mp-C_α, showing again the benefits of P doping increasing the photocatalytic activity for overall water splitting.

A comparison of the H_2 production in the overall water splitting and in the presence of methanol (Fig. S.14 in Supporting information) shows that the presence of sacrificial electron donor increases the efficiency in H_2 generation by a factor of about 6 times. This comparison indicates, as it has been frequently observed, that the slowest process in the overall water splitting should be H_2O oxidation by the valence band holes and when this process is decoupled from H_2O reduction, then H_2 generation rate increases substantially. On the other hand, the rate of overall H_2O splitting is a bit lower, but similar to that of photocatalytic O_2 evolution in the presence of Ce(IV) as electron acceptor.

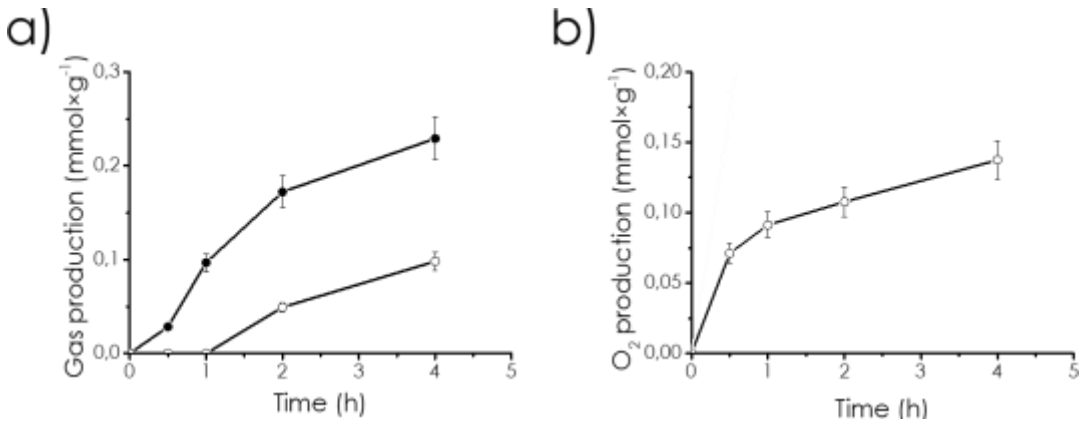

Fig 7. Gas production in a) overall water splitting reaction H_2 production (●) and O_2 production (○), and b) O_2 evolution using Ce^{IV} as electron acceptor. Reaction conditions: 20 mL of MilliQ H_2O in a reactor of 51 mL, 10 mg of (P)C_α-2, irradiation using 300 W Xe lamp at room temperature in the absence (plot a) or in the presence of 10^{-2} M of $Ce(NH_4)_2(NO_3)_6$.

Photodeposition

It is well-known that the photocatalytic activity of semiconductors can increase upon modification of the material by deposition of minor amounts of metals and metal oxides acting as co-catalysts.[5, 27, 28] These metal and metal oxide nanoparticles in contact with the semiconductor surface increase charge separation due to their role as charge carrier buffers or/and promote gas evolution derived from their catalytic activity. A general procedure to deposit these co-catalysts takes advantage of the occurrence of photoinduced charge separation to produce photocatalytic reduction or oxidation of water-soluble metal salts to deposit insoluble metal or metal oxide nanoparticles, respectively.[29] On the other hand,

observation by TEM of photodeposition of metal and metal oxide nanoparticles on the mp-(P)C is a strong evidence of the occurrence of charge separation.

Photodeposition of Pt nanoparticles on mp-(P)C_α was performed by irradiating with simulated sunlight an Ar purged aqueous solution of K_2PtCl_6 salt in water containing 20 vol.% of methanol as sacrificial electron donor. While control experiments using the same reagents and procedure in the dark do not reveal the formation of Pt nanoparticles on the mp-(P)C_α photocatalyst, photodeposition of small 1-2 nm Pt nanoparticles upon visible light irradiation was confirmed by TEM, EDS analyses and elemental mapping (Figs. S15 and S16 in supporting information). Fig. 8 shows selected TEM images of these Pt nanoparticles on the surface of mp-(P)C_α. This indicates that the photogenerated conduction band electrons reduce Pt^{VI} to Pt^0, while valence band holes become quenched by methanol.

Since Pt nanoparticles have a well-proven activity as co-catalysts for H_2 evolution, the photocatalytic activity of Pt/(P)C_α upon simulated sunlight irradiation in the presence of methanol as sacrificial electron donor was compared to that of (P)C_α under the same conditions. Fig. 8 presents the corresponding temporal profiles for Pt/(P)C_α-2 and (P)C_α-2 showing that Pt photodeposition enhances H_2 production.

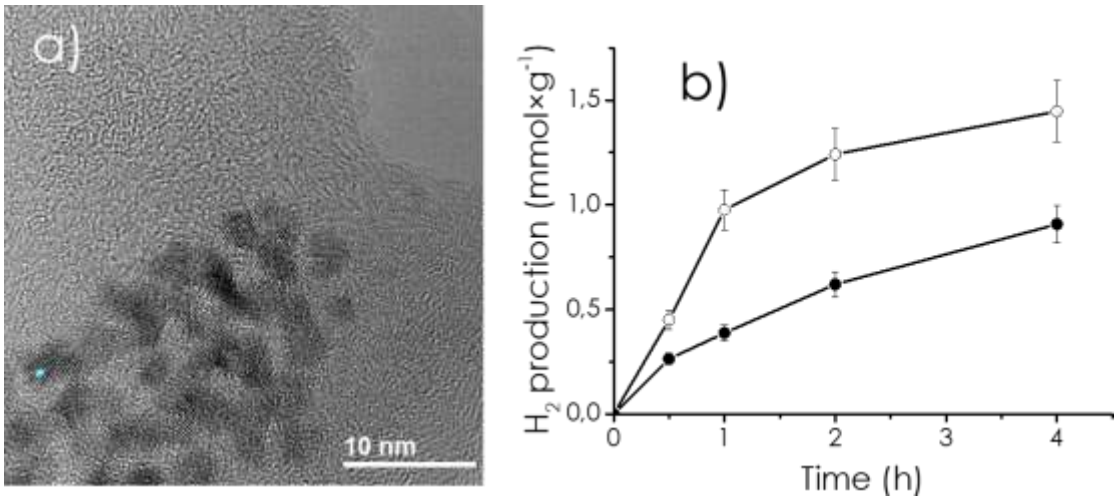

Fig 8. a) HRTEM images of the Pt nanoparticles formed upon photodeposition on mp-(P)C. b) H_2 production using electron donor in the presence of Pt/(P)C_α-2 (○) or (P)C_α-2 (●) as photocatalyst.

An analogous photodeposition experiment was performed under oxygen as electron acceptor using a 0.1 M aqueous solution of $CrCl_2$ to promote photooxidation to insoluble Cr_2O_3. Deposition of Cr_2O_3 on mp-(P)C_α was determined by EDS analysis (Fig. S.17 in Supporting information) and TEM images (Fig. 9). As expected in view of the activity of transition metal oxides as co-catalysts for O_2 evolution,[30, 31] Figure 9 shows that the photocatalytic activity of Cr_2O_3/(P)C_α in the presence of Ce^{IV} as electron acceptor was higher than that of mp-(P)C_α under the same conditions.

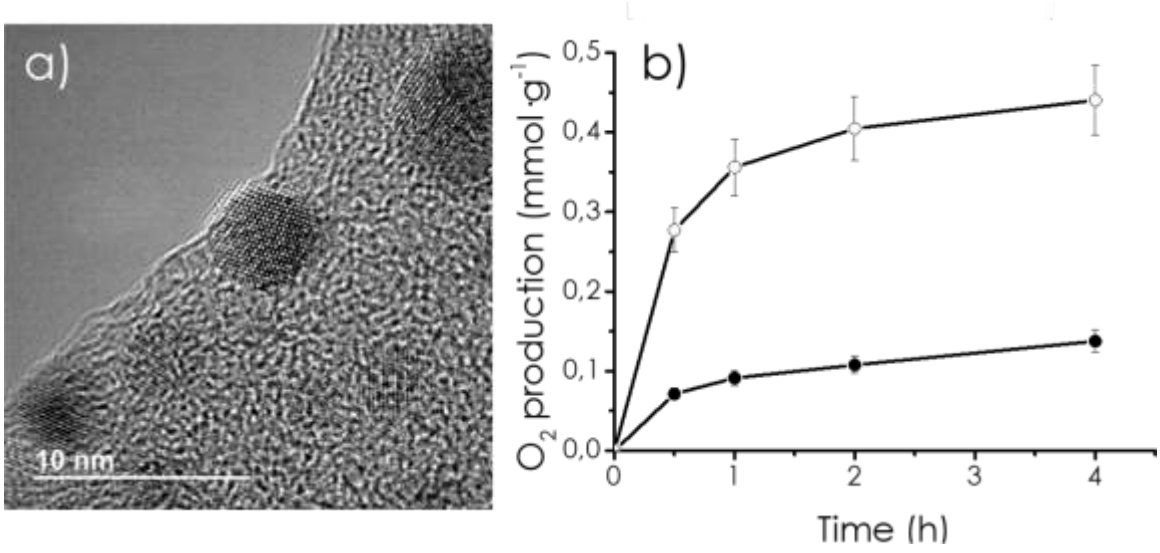

Fig 9. a) HRTEM images of the Cr_2O_3 nanoparticles on (P)C_α-2 formed by photodeposition upon illumination of a suspension of (P)C_α-2 in 10^{-2} M aqueous solution of $CrCl_2$ under air and b) O_2 production using Ce^{IV} as electron acceptor under irradiation using a 300 W Xe lamp ○) Cr_2O_3/(P)C_α-2 and ●) (P)C_α-2.

In comparison to the effect of Pt deposition that increases H_2 generation by a factor of 1.5, Cr_2O_3 deposition on (P)C_α-2 enhances the photocatalytic activity of (P)C_α-2 for O_2 evolution by a factor near 4.0. This higher relative increase in O_2 generation due to the presence of co-catalyst can be understood considering that O_2 evolution is kinetically the slowest semireaction, since it requires the removal of four electrons and four protons from two water molecules.

Photocurrent measurements

Cyclic voltammetry of (P)C_α in 1 M aqueous KCl electrolyte is presented in Fig. 10. The voltammogram shows a reduction peak at -0.95 V and an oxidation peak at +1.55 V vs. AgCl/Ag reference electrode that are probably related to the reduction and oxidation of sites involving dopant P and O elements of mp-(P)C_α. The discharge peaks corresponding to H_2 and O_2 evolution reactions from H_2O using (P)C_α-2 as electrode appeared with onsets at -1.55 and 2.10 V vs. AgCl/Ag.

A thin layer of (P)C_α deposited on transparent conductive FTO electrode exhibits photocurrent upon irradiation with UV-Vis light. The direct current follows the same sense as an analogous TiO_2 electrode, indicating that (P)C_α is a *n*-type semiconductor. Photo action spectrum of (P)C_α was recorded measuring the photocurrent upon monochromatic light illumination of the (P)C_α-FTO electrode showing a photoresponse in the UV region together with a visible peak between 450 and 700 nm with maximum photocurrent at 550 nm (Fig. 10). Regarding external quantum efficiency, it should be commented that the photoelectrodes were mostly transparent and visible absorbed light was mostly transmitted through the film, meaning that the efficiency should be much higher than that estimated in Fig. 10. Observation of this peak is in agreement with the visible light photocatalytic H_2 generation previously observed. Chronoamperometry showed that the photocurrent increased with the photoelectrode polarization potential in the range from 0.6 to 1.30 V, becoming saturated at increasing voltages (Fig. S18 in supporting information) and

diminishes in the presence of Ce^{IV} as competing electron acceptor (Fig. S19 in supporting information).

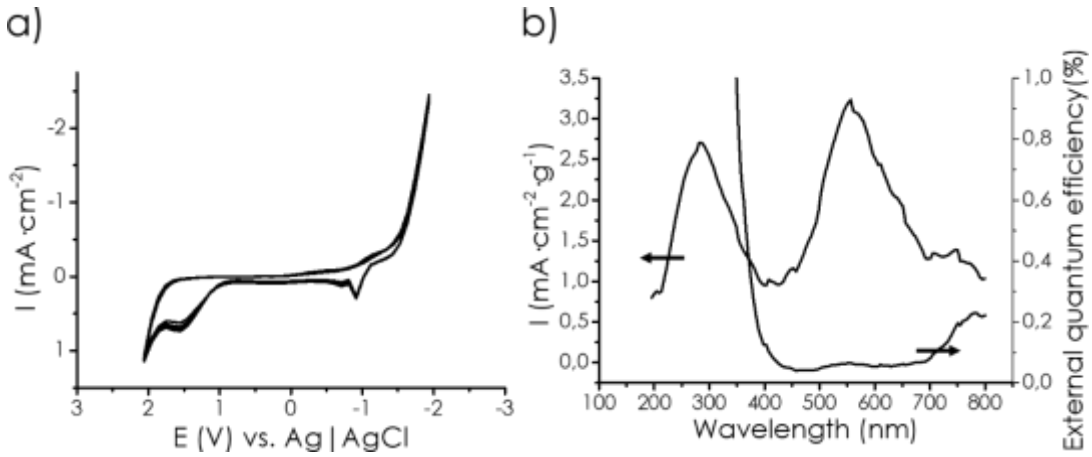

Fig 10. a) Cyclic voltammetry of (P)C_α–2 in 1 M KCl electrolyte and b) photoresponse (left axis) and external quantum efficiency (right axis) of a thin film of (P)C_α-2 deposited on FTO electrode. Measurement conditions: 1 M aqueous KCl electrolyte, scan rates 20 mV×s^{-1} (a) or 5 nm×s^{-1} (b), 500 W Xe lamp coupled with a Zolix Omni-λ300D monochromator.

Conclusions.

The present results have shown the possibility of band alignment in microporous graphitic carbons by P doping, diminishing the bandgap by increasing the energy of the valence band edge due to the contribution of P lone electron pairs. In this way, the photocatalytic activity for H_2 generation has been increased by about 5.5 times compared

to an analogous undoped sample. Using methanol as sacrificial electron donor, H_2 evolution of 2.5 mmol $g_{catalyst}^{-1}$ was achieved. Part of the photocatalytic activity derives from the visible region. The resulting P-doped particulate microporous carbon was photocatalytically stable and recyclable without observing any decay in activity according to the temporal H_2 evolution profiles. These P-doped microporous carbons also exhibit photocatalytic activity for overall water splitting upon simulated sunlight illumination with a production in the absence of cocatalysts of 225 μmol H_2 $g_{catalyst}^{-1}$ in 4 h. It was found that overall water splitting is limited by the O_2 evolution semireaction that increases by a factor of 5 when Cr_2O_3 was deposited as cocatalyst. These photocatalytic performance values are among the highest so far reported, with the additional benefit of being a metal-free material.

Experimental section

Synthesis of mp-(P)C_α

200 mg α-cyclodextrin (0.41 mmol, 972.8 g×mol^{-1}, Sigma-Aldrich) were dissolved in 20 mL of milliQ water. In constant agitation, different fractions of phosphoric acid (Sigma-Aldrich) were added to the cyclodextrin solution to obtain different percentages of phosphorous (2.5 μL, 12 μL and 25 μL for (P)C_α-1, (P)C_α-2 and (P)C_α-3, respectively). After 24 hours of vigorous stirring, the mixture was dried by heating at 60°C in a silicone bath. The white product was pyrolized heating at 10 °C ×min^{-1} up to 900 °C for 2 h with an electric oven. The graphenic material was milled and prepared for characterization and following tests.

For β-cyclodextrin (0.352 mmol, 1135 g×mol^{-1}, Sigma-Aldrich) and γ-cyclodextrin (0.308 mmol, 1297.12 g×mol^{-1}, Simma-Aldrich) the preparation procedure is the same as described above.

Photocatalytic tests

All the photocatalytic reactions were developed in a 51 mL quartz photoreactor fitted with a manometer, an inlet valve, and an outlet valve. The irradiation was carried out using a 300 W Xe lamp (Hamamatsu, 1,6 sun power) with UV-Vis light range or simulated sunlight irradiation (OrielTM, 1 sun power).

First, the photocatalyst was dispersed in 30 mL of water (1,5 mg×mL^{-1}) using a Sonic tip (FisherbrandTM Model 705 at 40% of 700 W for 1 hour using 1 s on 1 s off pulsation). After that, the necessary amount of suspension is introduced in the reactor, added 4 mL of methanol (Aldrich) (4:1 relation), as electron donor or triethanolamine (Aldrich), and MilliQ water until 20 mL of mixture. The system was purged with Ar for 10 min in order to remove the air of it before the irradiation.

In the case of O_2 evolution, $(NH_4)_2Ce(NO_3)_6$ (Aldrich) was added as electron acceptor in a concentration of 1 mM.

The gas phase was analyzed using a gas chromatograph (Agilent 490 MicroGC) equipped with a molecular sieve 5 Å column with TC detector and Ar as carrier gas.

Platinum photodepostion

For the Pt photodeposition, the photocatalyst was dispersed in 30 mL of MilliQ (1,5 mg×mL^{-1}) water using ultrasounds. 7,5 mL of this suspension were introduced in the reactor with 4 mL of methanol as electron donor and H_2PtCl_6 in a concentration of 0,1 mM. After 15 min of irradiation, the solid was recovered by centrifugation (Hettich Zentrifugen EBA 21) at 6000 rpm for 30 min. The supernatant was removed and the solid was washed several times with MilliQ water by centrifugation. The solid was used in a H_2 evolution reaction and characterized using HRTEM.

Chromium oxide photodeposition

On the other hand, for locating the holes, Cr photodeposition was carried out. In this case, as done previously, photocatalyst was dispersed in 30 mL of MilliQ water using ultrasounds in a concentration of 1,5 mg·mL^{-1}. 7,5 mL of this suspension were introduced in the reactor and 12,5 mL of MilliQ water with $CrCl_2$ 0,1 mM. After 15 min of irradiation using the Xe lamp, the suspension was centrifuged (Hettich Zentrifugen EBA 21) at 6000 rpm for 30 min. The supernatant was removed and the solid was washed with MilliQ water by centrifugation several times. The obtained material was characterized using HRTEM.

Photoelectrochemical measurements

Photoelectrochemical measurements were made in a conventional three-electrode electrochemical cell, using Ag/AgCl as reference electrode, Pt wire as auxiliary electrode that accompanies the P-doped graphene on Fluorine doped Tin Oxide (FTO) glass, as working electrode.

Voltammetric experiments were carried out using a potentiostatic devide Solatron, using an aqueous solution of KCl 1 M saturated with N_2 as electrolyte. The monocromator Zolix Omni-λ300D was used for irradiation.

Notice that the working electrode was prepared using the aPho50 with 1 % Paraloid dissolved in acetone as binder. For drying, the electrode was heated up to 50°C.

Physicochemical characterization

Raman spectra were recorded with 514 nm laser excitation on a Renishaw Raman spectrometer ("Reflex") equipped with a Leica optical microscopy and a charged coupled device camera. The laser power in the sample was 25 mW. Each spectrum was the average of 20 acquisitions at a resolution of 4 cm^{-1}.

Solid-state ^{31}P-NMR spectra were measured at room temperature using a Bruker AV400WB with $\pi/2$ pulse sequences of τ=5 μs and a relaxation time of 5 s. The experiments were carried out with Magic Angle Spinning on a rate of 10 kHz. For obtaining the spectra, between 100 and 400 scans were accumulated.

TEM images were recorded on a JEOL JEM 2100F with a voltage of 200 kV coupled with X-Max dispersive energy X-ray detector (EDX).

X-ray photoelectron spectroscopy (XPS) measurements were carried out in a XPS spectrometer SPECS, which includes a monochromatic X-ray source Al Kα1 (photonic energy 1486.74 eV), operating under ultrahigh vacuum at 1.3×10^{-13} atm. The binding energies were corrected for surface charge effects during measurements using the central level of C1s (284.5 eV) as internal reference.

The specific surface area was determined by the CO_2 adsorption-desorption isotherms with a Micromeritics ASAP 2020 equipment

The combustion elemental analyses were measured with a Euro EA 3000 analyzer. Thermogravimetric profiles were obtained using a Mettler Toledo TGA/SDTA 851 station at a temperature range of 25–900 °C with a scanning speed of 10 °C min^{-1} and a N_2 flow of 30 mL min^{-1}. XRD pattern was recorded using a Cubix-pro PANalytical diffractometer in the range from 5 to 90 o at a scan rate of 1 o$\times s^{-1}$.

Acknowledgments

Financial support by the Spanish Ministry of Science and Innovation (Severo Ochoa and RTI-2018-98237-CO2-R1) and Generalitat Valenciana (Promoteo 2017/063) is gratefully acknowledged. A. G. M. and A.P. also thank the Spanish Ministry of Science and Innovation by a postgraduate scholarship and a Ramón y Cajal research associate contract, respectively.

References

1. G. W. Crabtree, M. S. Dresselhaus and M. V. Buchanan, *Physics today*, 2004, **57**, 39-44.
2. A. Léon, *Hydrogen technology: mobile and portable applications*, Springer Science & Business Media, 2008.
3. Z. Wang, C. Li and K. Domen, *Chemical Society Reviews*, 2019, **48**, 2109-2125.
4. A. Fujishima and K. Honda, *nature*, 1972, **238**, 37-38.
5. K. Maeda and K. Domen, *The Journal of Physical Chemistry Letters*, 2010, **1**, 2655-2661.

6. Roskill, Critical materials: EU releases updated critical raw materials list, https://roskill.com/news/critical-materials-eu-releases-updated-critical-raw-materials-list/).
7. X. Wang, K. Maeda, A. Thomas, K. Takanabe, G. Xin, J. M. Carlsson, K. Domen and M. Antonietti, *Nature materials*, 2009, **8**, 76-80.
8. X. Wang, S. Blechert and M. Antonietti, *Acs Catalysis*, 2012, **2**, 1596-1606.
9. Q. Xiang, J. Yu and M. Jaroniec, *Chemical Society Reviews*, 2012, **41**, 782-796.
10. J. Albero, A. Vidal, A. Migani, P. Concepción, L. Blancafort and H. García, *ACS Sustainable Chemistry & Engineering*, 2018, **7**, 838-846.
11. Q. Xiang, B. Cheng and J. Yu, *Angewandte Chemie International Edition*, 2015, **54**, 11350-11366.
12. T.-F. Yeh, J. Cihlář, C.-Y. Chang, C. Cheng and H. Teng, *Materials Today*, 2013, **16**, 78-84.
13. C. Lavorato, A. Primo, R. Molinari and H. Garcia, *Chemistry–A European Journal*, 2014, **20**, 187-194.
14. D. Mateo, I. Esteve-Adell, J. Albero, J. F. S. Royo, A. Primo and H. Garcia, *Nature communications*, 2016, **7**, 1-8.
15. Y. Peng, A. Rendón-Patiño, A. Franconetti, J. Albero, A. Primo and H. Garcia, *ACS Applied Energy Materials*, 2020.
16. A. Rendón-Patiño, A. Santiago-Portillo, C. Vallés-Garcia, M. Palomino, S. Navalón, A. Franconetti, A. Primo and H. Garcia, *Small Methods*, 2020, **4**, 1900721.
17. L. K. Putri, W.-J. Ong, W. S. Chang and S.-P. Chai, *Applied surface science*, 2015, **358**, 2-14.
18. M. Latorre-Sánchez, A. Primo and H. García, *Angewandte Chemie International Edition*, 2013, **52**, 11813-11816.
19. A. C. Ferrari, J. Meyer, V. Scardaci, C. Casiraghi, M. Lazzeri, F. Mauri, S. Piscanec, D. Jiang, K. Novoselov and S. Roth, *Physical review letters*, 2006, **97**, 187401.
20. A. Primo, E. Sánchez, J. M. Delgado and H. García, *Carbon*, 2014, **68**, 777-783.
21. M. Latorre-Sanchez, P. Atienzar, G. Abellan, M. Puche, V. Fornés, A. Ribera and H. García, *Carbon*, 2012, **50**, 518-525.
22. G. Abellán, M. Latorre-Sánchez, V. Fornés, A. Ribera and H. García, *Chemical Communications*, 2012, **48**, 11416-11418.
23. J. Albero, D. Mateo and H. García, *Molecules*, 2019, **24**, 906.
24. C. Acar, I. Dincer and G. F. Naterer, *International Journal of Energy Research*, 2016, **40**, 1449-1473.
25. V. Kumaravel, S. Mathew, J. Bartlett and S. C. Pillai, *Applied Catalysis B: Environmental*, 2019, **244**, 1021-1064.
26. A. A. Ismail and D. W. Bahnemann, *Solar energy materials and solar cells*, 2014, **128**, 85-101.
27. J. Yang, D. Wang, H. Han and C. Li, *Accounts of chemical research*, 2013, **46**, 1900-1909.
28. J. Ran, J. Zhang, J. Yu, M. Jaroniec and S. Z. Qiao, *Chemical Society Reviews*, 2014, **43**, 7787-7812.
29. K. Wenderich and G. Mul, *Chemical reviews*, 2016, **116**, 14587-14619.
30. N. Wang, J. Li, L. Wu, X. Li and J. Shu, *International Journal of Hydrogen Energy*, 2016, **41**, 22743-22750.
31. D. Wei, Y. Ding and Z. Li, *International Journal of Hydrogen Energy*, 2020, **45**, 17320-17328.

GRAPHICAL ABSTRACT